New Pyrochlore-like Oxyfluorides Na2-2xSnxM2O5F2 (M = Nb5+ or Ta5+ and 1 ≤ x ≤ 0) as Potential Candidates for Overall Water Splitting Photocatalysis

Edouard Boivin, Sébastien Saitzek, François Fauth, Marielle Huvé, Pascal Roussel, Houria Kabbour

New pyrochlore-like oxyfluorides $SnM_2O_5F_2$ ($M=Nb^{5+}$ and Ta^{5+}) as potential candidates for overall water splitting photocatalysis.

Edouard Boivin[1*], Sébastien Saitzek[1], François Fauth[2], Marielle Huvé[1], Pascal Roussel[1], Houria Kabbour[1*]

1. *Univ. Lille, CNRS, Centrale Lille, ENSCL, Univ. Artois, UMR 8181-UCCS-Unité de Catalyse et Chimie du Solide, F-59000 Lille, France*
2. CELLS-ALBA Synchrotron, E-08290 Cerdanyola del Vallès, Barcelona, Spain

* edouard.boivin@univ-lille.fr , houria.kabbour@univ-lille.fr

Abstract

Lone pair containing oxyfluorides have recently emerged as efficient and stable photocatalysts for overall water splitting (OWS). In this work we have obtained several new potential OWS photocatalysts with pyrochlore structure (*i.e.* $Na_{2-2x}Sn_xM_2O_5F_2$ with $M=Nb^{5+}$ or Ta^{5+} and $1 \leq x \leq 0$) through kinetically controlled ion-exchange reaction from $Na_2M_2O_5F_2$. Rietveld refinement of the structures as well as DFT indicate the Sn^{2+} lone pair stereochemical activity. The partial density of states reveals contributions at the top of the valence band, which are mainly composed of a Sn 5s – Sn 5p hybridization through the (O,F) *2p* orbitals. This leads to a significant narrowing of the band gap and an improvement of the photoconduction response by a factor *ca.* 50 with respect to the x= 0 compound, $Na_2Nb_2O_5F_2$. The Mott-Schottky measurements show that all materials possess band edge positions encompassing the thermodynamic redox potential of H^+/H_2 and O_2/H_2O. However, the valence band of $SnNb_2O_5F_2$ may not be oxidative enough to overcome the overpotential associated to the O^{2-} oxidation and hence could be unsuitable for OWS photocatalysis in contrast with $Na_{1.5}Sn_{0.25}Nb_2O_5F_2$.

Introduction

Sunlight driven overall water splitting photocatalysts has attracted considerable attention for H_2 production as a clean energy carrier. Efficient solar energy conversion requires semiconductors with small bandgap (< 3 eV) in order to absorb the main component of solar spectrum. For this concern, metal oxides had first been explored as photocatalysts,[1–6] but it has been found to be difficult to design oxides possessing bandgap below 3 eV and with band edge positions suitable for both H^+ reduction and O^{2-} oxidation. Alternatively, oxynitrides have been extensively studied because of the more covalent M-N than M-O bonds interactions, and in which N 2*p* states contribute to Valence Band Maximum (VBM) above O 2p states narrowing the band gap without essentially affecting the Conduction Band Minimum (CBM).[7] However the main issue of these materials is their instabilities as photocatalysts, due to the oxidation of nitride anions leading to N_2 release.[8] More recently, oxysulfides, which also may exhibit narrower band gap compared to oxides, are seen as potentially suitable candidates.[9,10] Besides the fine control of the photon absorption properties by anionic mixing, heteroleptic

coordination geometries around the metal center may also allow to enhance the electron-holes transport properties thought local symmetry engineering.[7,11]

On contrary to oxynitrides and oxysulfides, oxyfluorides, in terms of visible-light-driven photocatalysis, may appear at first sight as unsuitable due to the high M-F bond ionicity that tend to increase the band gap. However, some pyrochlore oxyfluorides have recently emerged as efficient and stable OWS photocatalysts.[12,13] For instance, the pyrochlore $SnTiNbO_6F$ has a band gap in the visible range of 1.88 eV and band edge positions encompassing the H^+/H_2 and H_2O/O_2 redox potentials. In this material, it is the $5s^2$ of Sn^{2+} lone pair (hybridized with (O,F) 2p and Sn 5p), located at the edge of the valence band, which induces a smaller band gap than generally observed for oxyfluorides (*i.e.* without lone pair cations).[13] However, in this compound ($SnTiNbO_6F$), O^{2-}/F^- ordering leaves the d^0 metals in regular MO_6 environments while heteroleptic configurations would promote the electron-hole pairs separation.[14] On another hand, $Pb_2Ti_2O_{5.4}F_{1.2}$ provides a mixed anion environment for both Pb^{2+} and Ti^{4+} cations.[15] This compound possesses remarkable photocatalytic properties for overall water splitting under visible light irradiation thanks to (i) a small band gap (2.4 eV), (ii) distorted $Ti(O,F)_6$ octahedra and (iii) a large dielectric constant that drive the separation of the photogenerated electron/hole pairs.[15] This example highlights the interest of exploring pyrochlore oxyfluorides with fluorine in the d^0 metal coordination sphere as well as within the ns^2 cation environment.

To the best of our knowledge, no compound containing Sn, Nb (or Ta), O and F have been reported so far, and hence exploring the SnF_2-M_2O_5 (M=Nb^{5+} or Ta^{5+}) tie-line might be a successful strategy to obtain new phases. However, the low melting point of SnF_2 as well as the tendency of SnO to disproportionate make difficult the synthesis of such phases by conventional solid-state reactions. Soft topotactic chemistry such as ion exchange synthesis, for which the pyrochlore structure is suitable,[16] offer an interesting solution to overcome these issues. Here we report a Na^+/Sn^{2+} ion exchange synthesis approach that allow a fine control of the composition. From the recently discovered pyrochlore $Na_2M_2O_5F_2$ (M = Nb^{5+}, Ta^{5+}) oxy-fluorides - possessing an O/F distribution that imply mixed anion environments for both Na and d^0 metals[17] - several $Na_{2-2x}Sn_xM_2O_5F_2$ compositions (*i.e.* x≈1, x≈0.5 or x≈0.25) have been obtained by controlling the ion exchange reaction kinetic. In these materials the Sn $5s^2$ lone pair stereochemical activity, the Sn^{2+} content, the local $Sn^{2+}/Na^+/\square$ ordering and the disordered O/F distribution confer unprecedented crystallographic features as well as remarkable and tunable physical properties.

Experimental part

$Na_2M_2O_5F_2$ materials have been synthetized as reported previously.[17] Approximatively 1g of Sn containing phases has been obtained by ion exchange reaction from $Na_2M_2O_5F_2$ using $SnCl_2$ dissolved in absolute ethanol ([Sn^{2+}] = 2 M) under solvothermal conditions in a 23mL PTFE container filled at 67% at moderate temperatures (100 or 140°C) for 60h. Samples were washed with absolute ethanol several times to remove the excess of $SnCl_2$ and then dried at 60°C overnight.

Synchrotron X-ray powder diffraction (SXRPD) experiments were performed at the MSPD beamline of the ALBA synchrotron (Barcelona, Spain).[18] The samples were sealed in a 0.2 mm diameter capillary and data were collected using the MYTHEN position sensitive detector in Debye−Scherrer geometry at energy just below Sn K-edge (0.4344 Å wavelength)

over a 3−50° angular range (0.006° step) and total integration time of 5 min. Laboratory XRD analyses were performed at room temperature in a 2θ range of 10−120° with a scan step width of 0.02° using a D8 Advance A25 Bruker AXS diffractometer in Bragg−Brentano geometry equipped with a 1D LynxEye XE-T detector and a Copper anode. Rietveld refinements and Bond Valence Sum (BVS) calculations were performed using the Fullprof suite.[19]

X-Ray Fluorescence (XRF) spectra were collected using a Bruker S2 Ranger spectrometer equipped with a Pd source and an energy dispersive detector. The samples were mixed with 50 wt.% of cellulose and then pressed into pellet. The spectra were analyzed using the Spectra EDX software from Bruker.

TEM - Electron diffraction study was performed on a FEI Technai G2-20 twin TEM microscope. The powder was crushed and dropped in the form of alcohol suspension on carbon supported copper grids followed by evaporation under ambient condition.

The thermogravimetric analysis (TGA) where conducted on a TGA-92 thermobalance (Setaram) under argon. The evolved gases were monitored by an Omnistar quadrupole mass spectrometer (MS, Pfeiffer) by continuously scanning in the range 0 – 100 amu. In order to control the atmosphere, the whole thermobalance was evacuated and filled with the carrier gas before heating up the samples up to 950 °C at a rate of 5 K/min.

UV−vis diffuse reflectance spectra were collected at room temperature using a PerkinElmer Lambda 650 spectrophotometer in the 200−800 nm range. Before the measurement, the blank was measured using $BaSO_4$ (standard for 100% reflectance) in order to calibrate the device. The reflectance spectra are converted to apparent absorption spectra using the Kubelka−Munk function, $\alpha = (1 - R)^2/2R$. The Zanatta's method[20], allowing a better estimation of the band gap (Eg) of polycrystalline materials than the Tauc plot, has been used to determine Eg. Indirect band gap is estimated as follows: $Eg = E^{BOLTZ} - 4.3\ \delta E$. Where E^{BOLTZ} is the energy coordinate at which the absorption coefficient $\alpha(E^{BOLTZ}) = (\alpha_{min} + \alpha_{max})/2$; α_{min} and α_{max} stand for the minimum and maximum of the absorption coefficient and δE is used to fit the profile of the α(E) curve near the absorption edge using the following equation:

$$\alpha(E) = \alpha_{max} + \frac{\alpha_{min} - \alpha_{max}}{1 + ex\ \left(\frac{E - E^{BOLTZ}}{\delta E}\right)}$$

Photo-electrochemistry. Transient photocurrents measurements and Mott-Schottky plots were carried out using a potentiostat/galvanostat coupled with Electrochemical Impedance Spectroscopy (EIS) module (PGSTAT204 -FRA32M, Metrohm). The photoelectrochemical cell (MM-PEC 15mL single sided-Magnetic Mount, Redox.me®) is made up from the pyrochlore sample coated on an ITO glass (delta technologies, LTD) as the working electrode, immersed in an electrolyte of an aqueous solution of 0.1 M of Na_2SO_4 (pH = 6.6). A platinum electrode and a standard Ag/AgCl electrode were used as counter electrode and as a reference electrode, respectively. To form the working electrode, the crushed powder is added to a mixture of water and N,N-Dimethylformanmide (DMF) solvents with 1:1 ratio. The paste obtained is then deposited on the ITO/glass substrate by the drop casting method and

dried at 80°C during few minutes in order to obtain a uniform layer. All the measurements were controlled with the Nova2.0 software allowing to regulate the excitation wavelength of different LEDs with low spectral dispersions (450, 470, 505, 530, 590, 617, 627 and 655 nm) as well as the luminous flux (from 0 to 126 mW / cm²).

Density Functional Theory (DFT) calculation were carried out by employing the projector augmented wave (PAW)[21,22] method encoded in the Vienna ab initio simulation package (VASP)[23] and the generalized gradient approximation of Perdew, Burke and Ernzerhof[24] (PBE) for the exchange-correlation functionals. The calculations were carried out on the Ta- and Nb-phase using a similar ordering scenario. Owing to the partially disordered character of the O/F distribution of experimental structure, a peculiar anionic and cationic distributions have been picked up among the possible configurations (see text for more details). Geometry optimizations at fixed unit cell parameters were carried out using a plane wave energy cutoff of 550 eV and 30 *k* points in the irreducible Brillouin zone. It converged with residual Hellman-Feynman forces on the atoms smaller than 0.03 eV/Å. The relaxed structures were used to calculate accurate electronic structure. For the later, the plane wave cutoff energies of 550 eV and the threshold of self-consistent-field energy convergence of 10^{-6} eV were used, with 163 *k* points in the irreducible Brillouin Zone. The ELF (Electron Localization Function) was also computed and allows the visualization of the nodal structure of the molecular orbital, including Lone Pair electrons.[25] We use it for the Sn^{2+} lone pair analysis.

Results

Synthesis and characterization

A^+/Sn^{2+} ion exchange in pyrochlore $A_2B_2X_6X'$ has, so far, been reported only in anion deficient pyrochlores (X'=□ or $O_{1-x}□_x$).[26] Indeed, the full occupancy of 8b site of the Fd-3m space group (*i.e.* X' site of pyrochlore) is known to hamper the diffusion of such a divalent cation within the pyrochlore channels. In anion deficient pyrochlore, the ion exchange can be initiated at room temperature while from $Na_2M_2O_5F_2$ materials, the full Na^+/Sn^{2+} exchanges can be achieved only thanks to a gentle heating in a sealed PTFE container. Under such conditions the use of $SnCl_2$ in absolute ethanol is required to provide a high enough solubility (544 g/g of ethanol at 23°C, while SnF_2 is sparingly soluble) as well as to avoid the hydrolysis of the Sn^{2+} salt in aqueous media ($SnCl_2$ + 2 H_2O give insoluble $Sn(OH)_2$ + 2 HCl). The ion-exchange synthesis has been carried out at either 100°C or 140°C from either $Na_2Nb_2O_5F_2$ or $Na_2Ta_2O_5F_2$ to yield four samples for which the cationic ratio obtained by X-Ray Fluorescence (XRF) are reported in **Table S1** and the X-Ray Diffraction (XRD) patterns are displayed in the **Figure 1.** Samples obtained at 140°C are both almost fully substituted and hence have compositions close to $SnNb_2O_5F_2$ and $SnTa_2O_5F_2$ while the composition of samples obtained at 100°C can be estimated to be approximatively $Na_{1.5}Sn_{0.25}Nb_2O_5F_2$ and $Na_1Sn_{0.5}Ta_2O_5F_2$. All along this article, the materials will be named as analysed from XRF, although their compositions may slightly differ from these estimations. Also, all samples contain a small amount of Nb_2O_5 or Ta_2O_5 impurity, already present in the starting powders. TGA-MS under inert atmosphere shows that the materials are stable only up to 450-500°C, temperature at which fluorine starts to be lost (**Figure S1**), even though they loss a small amount of H_2O and CO_2 at lower temperature. It indicates that these compounds obtained by ion-exchange at low

temperature are metastable and it could not be synthesized using standard solid-state reaction.

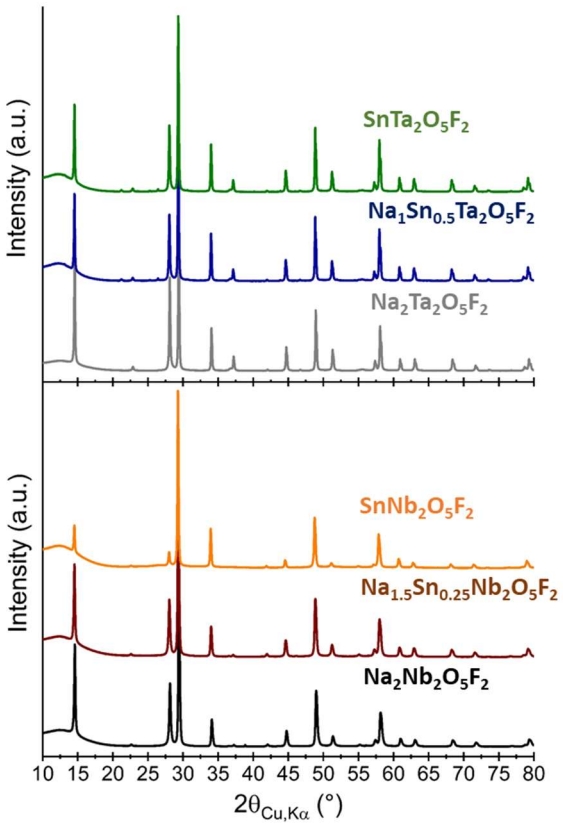

***Figure 1**: XRD patterns of the $Na_{2-2x}Sn_xM_2O_5F_2$ compounds obtained by ion exchange synthesis from the pyrochlore $Na_2M_2O_5F_2$ (M=Nb or Ta).*

Crystallographic structure

Although ion-exchange syntheses usually lead to topotactic reactions, the large difference in the nature of the cations exchanged (Na^+ by Sn^{2+}) in terms of electro-negativity, size, charge, electronic configuration *etc.* requires a careful analysis of the crystal structure of the obtained materials. Several other pyrochlore-like oxy-fluorides containing lone pair cations and d^0 transition metals have already been reported to deviate from the ideal pyrochlore structure.[14,15] For instance, in $Pb_2Ti_2O_{5.4}F_{1.2}$ the distortion of Ti^{4+} octahedra allowed by the F-43m space group is driven by the partial O/F ordering conferring to TiO_3X_3 (X= 60% O 40% F) a cis configuration while Pb^{2+} is displaced along the [111].[15] Between Fd-3m and F-43m space groups, the reflection conditions differ slightly. For instance, the h00 reflections with h = 2n are allowed in F-43m but forbidden in Fd-3m (where only h = 4n are allowed). Therefore, electron diffraction (ED) has been employed, in order to identify the space group of $SnM_2O_5F_2$ materials (see **Figure 1**). The electron diffraction patterns along the [100] zone axis, shown **Figure S2**, reveal only the presence of the h = 4n reflections indicating a Fd-3m space group for these materials, as also observed in Sn_2TiNbO_6F, for instance.[14] Therefore, the structural refinements of the structure of $SnNb_2O_5F_2$ and $SnTa_2O_5F_2$ against synchrotron XRPD data have first been performed in the Fd-3m space group with Sn in a half occupied 16d position and Nb or Ta in the 16c Wyckoff site. The partial O/F ordering identified in the parent compounds (*i.e.* 8b site fully occupied by F^- and the 48f site statistically occupied by 83% of O^{2-} and 17% of F^-)[17] has been considered as unchanged in the ion exchanged phases.

However, this model led to large U_{iso} for Sn and F which would indicate a displacement of these atoms in lower symmetry Wyckoff positions. Indeed, the Fourier map reveals four lobes centred on 8b position suggesting the localisation of fluorine on the 32e site (*i.e.* x, x, x), instead of 8b (3/8, 3/8, 3/8) (see **Figure S3**). Moreover, the observed electronic density around the 16d position indicates that Sn occupies the 96g (x,x,y) and not the 96h (0,y,-y) Wyckoff position observed in Sn_2TiNbO_6F.[14] The displacement of Sn^{2+} away of the central 16d position allows the 442 Bragg reflection of the Fd-3m space group (forbidden for Sn in 16d position), as observed in the **Figure S3** and indicates the stereochemical activity of the Sn^{2+} lone pair in these materials.[27] The results of the Rietveld refinement are displayed in the **Figure 2**, the refined parameters and agreement factors are summarized in the **Table 1** and the structure is displayed in the **Figure 3a** and **3b.**

***Table 1**: Refined structural parameters of $SnNb_2O_5F_2$ and $SnTa_2O_5F_2$ obtained from Rietveld refinement of the structures against SXRPD data. The Bond Valence Sum (BVS) are also given, calculated from ref.*[28]

$SnNb_2O_5F_2$								
SG : *Fd-3m* Z = 8 Purity > 99 w%			*a* = 10.5577(1) Å				R_{Bragg} = 2.10 % R_{wp} = 3.29 % χ^2 = 14.2	
Site $^{\Delta}$	Atoms	Wyckoff position	*x*	*Y*	*Z*	Occupancy*	U_{iso}	BVS
A	Sn	*96g*	0.4801(2)	0.4801(2)	0.5262(3)	0.960(8)	0.014(2)	1.64(2)
B	Nb	*16c*	0	0	0	2	0.009(1)	4.82(1)
X	O	*48f*	0.3162(1)	⅛	⅛	5.020(9) [1]	0.017(1) [2]	1.79(1)
X	F	*48f*	0.3162(1)	⅛	⅛	1.004(9) [1]	0.017(1) [2]	1.61(1)
X'	F'	*8b*	⅜	⅜	⅜	0.166(6)	0.022(2) [3]	0.74(1)
X'	F''	*32e*	0.348(2)	0.348(2)	0.348(2)	0.756(5)	0.022(2) [3]	0.68(1)

$SnTa_2O_5F_2$								
SG : *Fd-3m* Z = 8 Purity > 95 w%			*a* = 10.5471(1) Å				R_{Bragg} = 1.71 % R_{wp} = 4.80 % χ^2 = 32.4	
Site $^{\Delta}$	Atoms	Wyckoff position	*x*	*y*	*z*	Occupancy*	U_{iso}	BVS
A	Sn	*96g*	0.4773(3)	0.4773(3)	0.5195(4)	0.914(8)	0.014(2)	1.48(2)
B	Ta	*16c*	0	0	0	2	0.006(1)	5.05(1)
X	O	*48f*	0.3146(3)	⅛	⅛	5.030(8) [1]	0.009(1) [2]	1.80(1)
X	F	*48f*	0.3146(3)	⅛	⅛	1.006(8) [1]	0.009(1) [2]	1.59(1)
X'	F'	*8b*	⅜	⅜	⅜	0.060(8)	0.015(1) [3]	0.89(2)
X'	F''	*32e*	0.354(1)	0.354(1)	0.354(9)	0.798(5)	0.015(1) [3]	0.86(1)

* Occupancy = site occupancy x site multiplicity / Z.

$^{\Delta}$ site refers to the $A_2B_2X_6X'$ formula of pyrochlores.

[1] the O/F ratio on the 48f site has been fixed to 5/1 and the overall occupancy has been refined

[2,3] These parameters have been refined together.

In the literature, the stoichiometry of tin (II) niobate and tantalate pyrochlores obtained by conventional solid-state reaction has been reported to be difficult to control especially due to the SnO disproportionation at rather low temperature, leading to non-stoichiometric materials with mixed Sn^{4+}-Nb^{5+}/Ta^{5+} occupancy of 16c site, inducing Sn^{2+} vacancies in the pyrochlore channel as well as anionic vacancies for the charge compensation.[14,29] The consideration of a mixed Sn^{4+}/M^{5+} occupancy on the 16c site didn't

lead to any significant deviation from the full occupancy of this site by M^{5+}. As a small Sn^{4+} in pyrochlore cannot be accommodated on the large A site, the average oxidation state of Sn must be very close to 2+, in good agreement with BVS (see **Table 1**). However, the refinement of atomic occupancies led to a slight deviation from the SnM_2X_7 composition (*i.e.* $Sn_{0.96(1)}Nb_2O_{5.02(1)}F_{1.00(1)}F'_{0.17(1)}F''_{0.76(1)}$, $Sn_{0.91(1)}Ta_2O_{5.03(1)}F_{1.01(1)}F'_{0.06(1)}F''_{0.80(1)}$) with few Sn^{2+} vacancies on the 96g site – which are not compensated by Na occupancy on the 16d position – associated to approximatively twice more anionic vacancies on the X' sites. This indicates that, based on the charge balance and despite the creation of fluorine vacancies (*i.e.* changes in overall O/F ratio), no significant F^- by O^{2-} replacement occurs during the synthesis. This agrees with the BVS values associated to O, F, F' and F'' indicating that the partial O/F ordering (fully fluorinated anti-cristobalite-type sublattice and disordered O/F distribution on the 48f site) observed in the pristine material might be preserved. Therefore, it clearly appears that the low temperature synthesis strategy that we report here allow a much better control of the Sn oxidation state, anionic stoichiometry as well as Sn/Nb anti-site defects than solid state reactions. Moreover, the kinetic control of the ion exchange reaction allows to tailor the Na^+/Sn^{2+} substitution level. Indeed, while the fully substituted materials are obtained at 140°C, intermediate compositions have also been obtained at lower temperature: $Na_{1.5}Sn_{0.25}Nb_2O_5F_2$ and $Na_1Sn_{0.5}Ta_2O_5F_2$, at 100°C. For these materials, the results of Rietveld refinements are displayed in the **Figure S4** and summarized in **Table S2**.

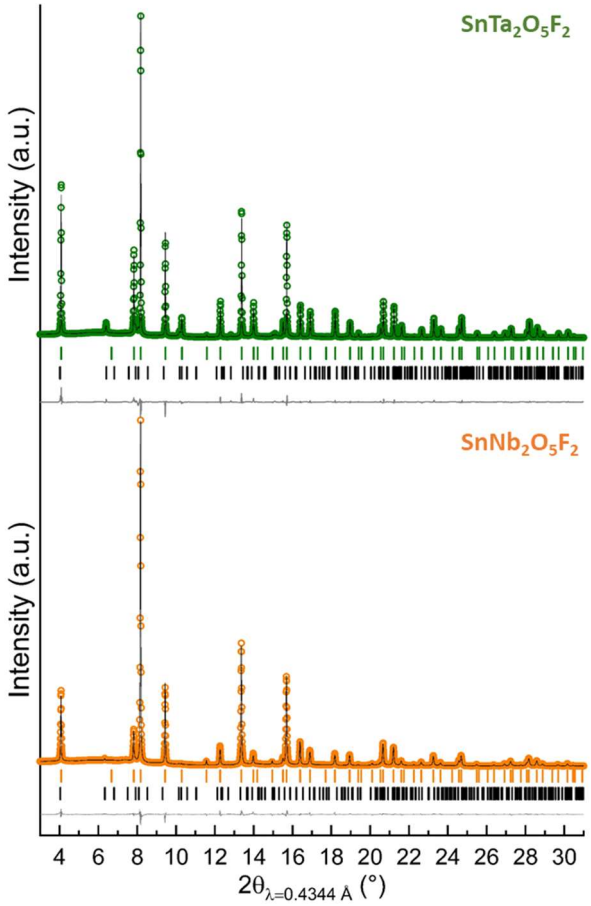

***Figure 2**: Rietveld refinement of the structures against synchrotron XRD data. The orange ($SnNb_2O_5F_2$) and green ($SnTa_2O_5F_2$) dots correspond to the experimental diffraction patterns, the black curves are the calculated diffraction patterns and the grey curves are the difference plots. The black tick marks indicate Bragg peaks of the Nb_2O_5 (<1 w%) or Ta_2O_5 (<5 %w) impurities.*

The significant increase of the lattice parameter with increasing tin content is unexpected considering only the effective ionic radius of Sn^{2+} (1.22 Å, [8]) similar to that of Na^{+} (1.16 Å, [8])[30] as well as the cationic vacancies created by the exchange of 2 Na^{+} by 1 Sn^{2+}. However, one has to account for the $5s^2$ lone pair stereochemical activity of Sn^{2+} which might increase the cell parameter and especially in an ionic fluorine-rich environment. Indeed, it is well established that the stereo-chemical character of Sn $5s^2$ lone pair decreases across the chalcogenide series, from SnO to SnTe (*i.e.* from ionic to covalent Sn-X interaction), and hence ionicity promotes acentric electronic distribution and expands the lone pair volume.[31,32] It's also important to note that the volume expansion associated to the exchange of 2 Na^{+} by 1 Sn^{2+} is higher in the Nb-based materials compared to the Ta-based phases (+0.4% *vs.* +0.2% per incorporated Sn^{2+}). This could indicate differences in the lone pair volume in both systems, although the average off-centering of Sn in the $SnX_6X'_2$ polyhedra (0.40(2) Å for Nb vs. 0.42(1) Å for Ta) are of the same order of magnitude.

In both materials, the displacement of F around the central 8b (≈0.6 Å) could not be only driven by the cooperative displacement of Sn/F due to the $5s^2$ lone pair stereochemical activity, as observed for instance in Sn_2TiNbO_6F,[14] but also by the local environment of the fluorine which is composed of two Sn and two vacancies, in average. Indeed, in the ordered α-$Ca_{1.5}\square_{0.5}Nb_2O_6F$ pyrochlore-like structure (S.G. $P4_332$), the $Ca^{2+}/\square$ ordering drives the fluorine off-centring away of the 3-fold axis and towards the three Ca^{2+} in the $FCa_3\square$ tetrahedra.[33]

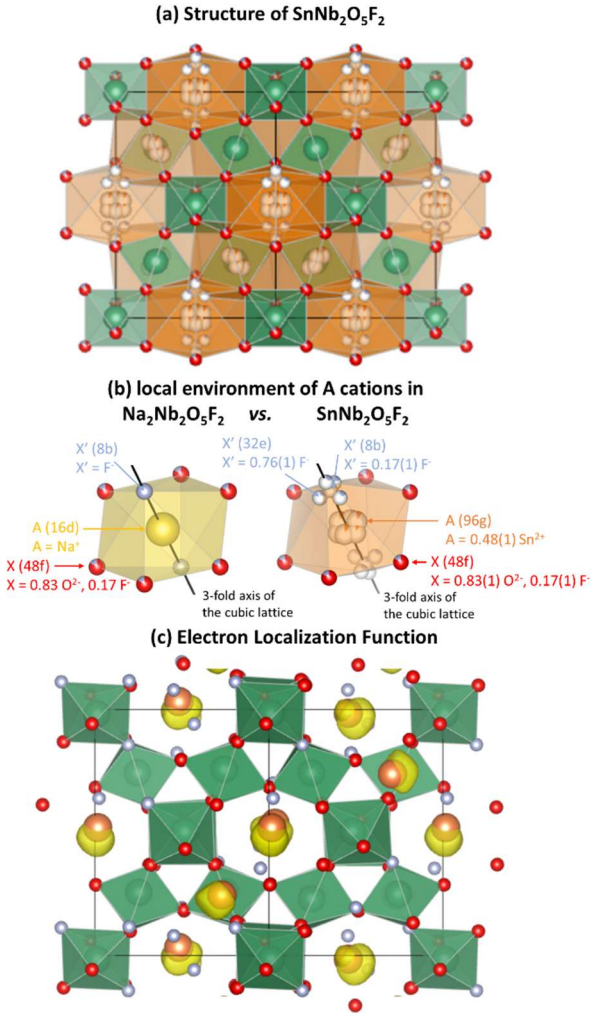

Figure 3: *Structure of $SnNb_2O_5F_2$ (a) and comparison of its local A site environment with the one observed in $Na_2Nb_2O_5F_2$ (b). Relaxed Structure obtained from DFT calculation and localization of the Sn^{2+} lone pair obtained with ELF (c).*

Although the synchrotron diffraction study of the materials gives plenty of useful information, it is only an average description of the structure. However, due to the static disorder on the A (position splitting and Sn/□ mixed occupancy) and X' (F distributed on both 32e and 8b positions) as well as X (disordered O/F distribution) sites, X-rays diffraction do not allow to properly describe the impact of the ligands distribution on the Sn^{2+} environment. For this concern, DFT calculations have been conducted. For our DFT models, we have selected one peculiar Sn/□ distribution on the A site that implies all X' anions being surrounded by two Sn^{2+} and two vacancies. In the starting model, tin has been located in the central 16d position and it could move away from this position during the structural optimization process. Also, an O/F and a Sn/□ distribution on the X and A sites have been selected in such way that the value of x in $SnO_{6-x}F_{2+x}$ polyhedra varies from 0 to 2. The details of the Sn-O/F distances in the relaxed DFT structures of $SnNb_2O_5F_2$ and $SnTa_2O_5F_2$ are shown in the **Table S3**.

The relaxed DFT structures have been examined and compared with the average structures determined by XRD. Both Sn and F' have been displaced away from their high symmetry 16d and 8b positions with average displacement close to that observed by diffraction. All BVS in the relaxed DFT model are in much better agreement with the expected

oxidation states than those determined from the average structure obtained by XRD. The Electron Localization Function technique – allowing to visualize $5s^2$ lone pair of Sn^{2+} - indicates that there is a clear cooperative Sn^{2+} displacement associated to the lone pair expression in the opposite direction (**Figure 3c**). Moreover, along the [-Sn-F'-Sn-F'-] sequences, the lone pairs form helicoidal patterns, tending alternatively towards X or X' and without any obvious preference for X site being occupied by O or F.

This detailed structural study combined with DFT calculation has revealed the Sn lone pair stereochemical activity which, according to the revised lone pair model,[31,32] plays a crucial role on the band structure nearby the Fermi level that we have investigated using UV-vis diffuse reflectance, Mott-Schottky measurement and DFT.

Electronic structure

The optical band gap of the two fully exchanged and of the two intermediate pyrochlore oxyfluorides have been estimated based on UV-Visible diffuse reflectance spectra (**Figure 4a**). The Zanatta's method[20] has been used to determine the band gaps, as described in the experimental section. Assuming indirect transitions (as also observed for $Sn_2Nb_2O_7$)[34], Eg is 2.35 and 3.22 eV for $SnNb_2O_5F_2$ and $SnTa_2O_5F_2$, respectively (see **Figure S5**). This is in good agreement with the yellow/orange and beige colors of the samples which contrasts with the white pristine powders (Eg = 3.99 eV for $Na_2Nb_2O_5F_2$ and 4.11 eV for $Na_2Ta_2O_5F_2$). The intermediate compositions, $Na_{1.5}Sn_{0.25}Nb_2O_5F_2$ and $Na_1Sn_{0.5}Ta_2O_5F_2$, obtained at lower temperatures, have band gaps of 2.71 eV and 3.29 eV, respectively. By comparing the fully exchanged, the intermediates, and the pristine compounds, it appears that most of the band gap narrowing upon Sn^{2+} incorporation occur at *x* below 0.5 in $Na_{2-2x}Sn_xM_2O_5F_2$, then the modification of the band gap is subtle. Although it is well known that lone pair cations tend to decrease the band gap in pyrochlore compounds, this is to the best of our knowledge, the first report showing the control of the band gap with Sn^{2+} content. Interestingly, as the full $Na_{2-2x}Sn_xM_2O_5F_2$ solid solution could be stabilized using this synthesis process, other Sn contents and hence band gaps could be obtained by an even finer control of the reaction kinetic.

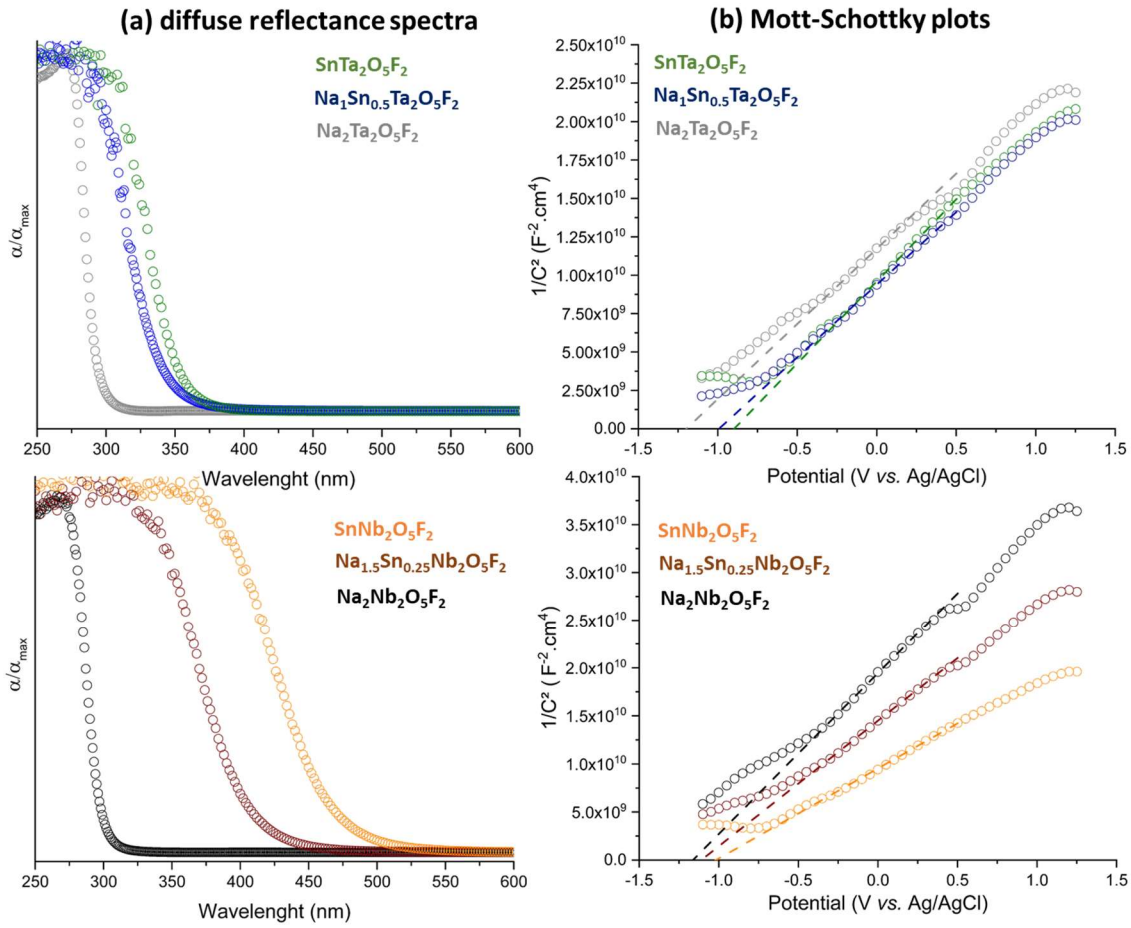

Figure 4: (a) diffuse reflectance spectra and (b) *Mott-Schottky plots of* $Na_{2-2x}Sn_xTa_2O_5F_2$ (top panels) *and* $Na_{2-2x}Sn_xTa_2O_5F_2$ (bottom panels).

In order to further understand the band gap narrowing mechanism in $SnNb_2O_5F_2$ and $SnTa_2O_5F_2$ oxyfluorides, the electronic structure have been calculated from the relaxed structures described above (see **Figure 5** and **Figure S6**). Smaller indirect band gaps than experimental ones (1.6 eV for Nb and 2.2 eV for Ta) are obtained from DFT, in good agreement with experiment regarding the expected underestimation of the GGA method. As reported previously, in the pristine $Na_2M_2O_5F_2$ compounds, at the bottom of the conduction band, M *nd* states are dominating and the top of the valence band is dominated by O 2*p* states.[17] In the Sn containing phases, this topology is mostly preserved but the valence band shows additional features. Indeed, additional valence states just below the Fermi level, separated by *ca.* 1 eV from the rest of the valence band are observed. The enlargement of this region, shown at the **Figure 5b**, reveals that they are mainly composed of Sn 5s - (O,F) 2p – Sn 5p hybridization, as observed in most of the lone pair cations containing pyrochlores.[35] This is due to the lone pair stereochemical activity inducing the distortion of the Sn site which, in return, allows the Sn $5s^2$ - (O,F) 2p – Sn 5p hybridization (forbidden for centro-symmetric Sn site) while the broad contributions of the "non-hybridized" Sn 5s and Sn 5p are localized between -2 and -8 eV.[31,32] Despite the presence of less fluorine than oxygen in the Sn environment (*i.e.* SnO_5F_3, in average), the fraction of F 2p electron involved in these Sn 5s – (O,F) 2p – Sn 5p hybridized states is *ca.* 30% higher than O 2p electrons (**Figure 5b**). This can be explained by the fact that it is the X' rather than the X anions which mostly contributes to this hybridization (see **Figure**

5c) and as soon as X' sites are exclusively occupied by fluorine, the contribution from oxygen appears to be much smaller. Although counterintuitive at a first sight, the highly electronegative fluorine overlaps more strongly with Sn orbitals than the more electropositive oxygen. However, in the context of the lone pair formation, this is consistent with the fact that a more ionic character would lead to a greater expression of the lone pair, as previously shown in the Tin chalcogenide series by Walsh *et. al*. [31,32] This also explain the important contribution of fluorine in this particular range just below the Fermi level where the states associated to the lone pair are found. We note that within the main valence block the trends are as expected for the F and O 2p states.

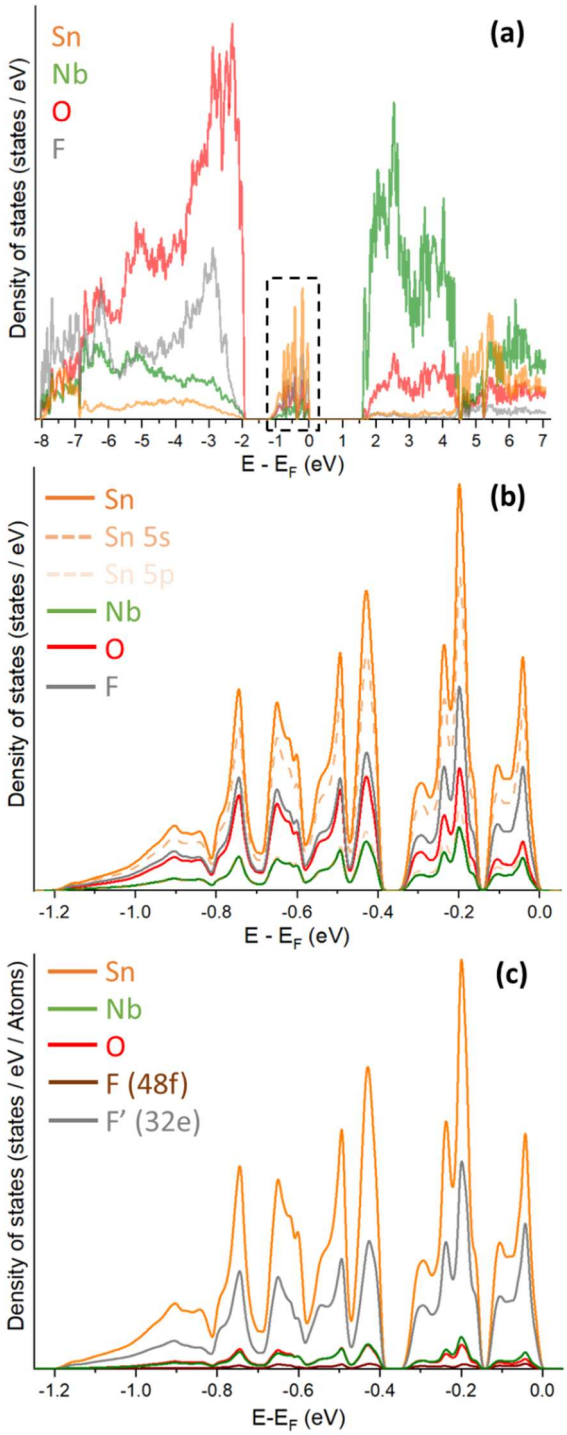

***Figure 5**: (a) PDOS of $SnNb_2O_5F_2$ with (b) the enlargement of the [-1.2 eV – 0 eV] region mainly composed of Sn 5s – (O,F) 2p – Sn 5p hybridized states and (c) the contributions to this region of the different crystallographic sites showing that X' anion (F, 32e site) more strongly overlap with Sn orbitals than X anions (O/F, 48f site).*

On another hand, $SnNb_2O_5F_2$ has a smaller band gap than $SnTa_2O_5F_2$ ($\Delta Eg \approx 0.9$ eV). It has been previously proposed that the larger band gap observed in Ta-based compounds is due to the fact that the CBM of the Ta system is much more negative than the Nb system (by ~0.7 eV), due to the significant contribution of higher energy Ta 5d orbitals instead of Nb 4d.[36] However, the Mott-Schottky measurements that we carried out (see **Figure 4b**) do not verify

this hypothesis. The plots evidence linear domains with positive slopes for all materials which is typical for n-type semiconductors, and with flat band potentials varying from -1.18 to -1.06 V vs. Ag/AgCl for $Na_{2-2x}Sn_xNb_2O_5F_2$ and from -1.19 to -0.89 V vs. Ag/AgCl for $Na_{2-2x}Sn_xTa_2O_5F_2$. The quasi-invariance of the flat band potential in $Na_{2-2x}Sn_xNb_2O_5F_2$ series is in rather good agreement with the presence of new valence states at the top of the VBM that leaves the CBM energy quasi unchanged and reduces the band gap by raising the VBM energy. A much subtler increase in the VBM energy is observed in the $Na_{2-2x}Sn_xTa_2O_5F_2$ series which is also in good agreement with the smaller impact of the Sn^{2+} incorporation on the band gap.

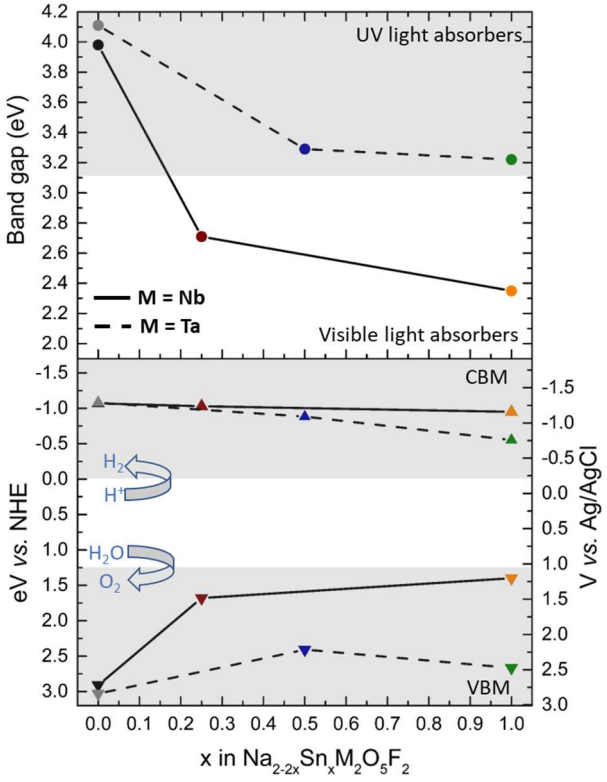

***Figure 6**: Evolution of band gap (top panel) and band edge position (bottom panel) as a function of x in $Na_{2-2x}Sn_xM_2O_5F_2$ series obtained from UV-vis diffuse reflectance spectra and Mott-Schottky measurements.*

In n-type semiconductors, the flat band potential is localized at approximatively 0.1 eV below the CBM.[37] From the Mott-Schottky plots E_{CBM} ($SnNb_2O_5F_2$) = -0.95 V and E_{CBM} ($SnTa_2O_5F_2$) = -0.78 V *vs.* H^+/H_2 at pH=0 and hence the corresponding VBM energy are E_{VBM} ($SnNb_2O_5F_2$) = 1.40 V and E_{VBM} ($SnTa_2O_5F_2$) = 2.67 V (see **Figure 6**). Although these band edge positions encompass well the thermodynamic values of H^+/H_2 and H_2O/O_2 redox potentials, the valence band of $SnNb_2O_5F_2$ might not be oxidative enough to overcome the overpotential associated to the O^{2-} oxidation and hence might not be suitable for overall water splitting. However, playing with the kinetic of the Na^+/Sn^{2+} ion exchange reaction allowed us to obtain a range of materials, including $Na_{1.5}Sn_{0.25}Nb_2O_5F_2$, which band edge positions are well located for overall water splitting photocatalysis (E_{VBM} = 1.68 V and E_{CBM} = -1.03 V *vs.* NHE). This is also the case for all the Ta-based oxyfluorides reported here, but the Sn incorporation has a lower effect on the band gap and even the fully substituted material, $SnTa_2O_5F_2$, absorbs only a small fraction of the visible light.

In order to further evaluate their performance for such an application the photocurrent generation under light irradiation was investigated. The transient photocurrent response as a function of the wavelength (from 450 nm to 655 nm) and measured at a bias voltage of 0.8 V *vs.* Ag/AgCl electrode for the $Na_{2-2x}Sn_xNb_2O_5F_2$ series is shown in **Figure 7** and in **Figure S7** for $Na_{2-2x}Sn_xTa_2O_5F_2$ materials. The variation of photocurrent density between dark and light (*i.e.* Δj) clearly decreases when the wavelength increases until no significant current density is detected at wavelengths corresponding to smaller energy than the band gaps 590 nm (2.10 eV *vs.* Eg = 2.35 eV for $SnNb_2O_5F_2$) and 505 nm (2.45 eV *vs.* Eg = 2.71 eV for $Na_{1.5}Sn_{0.25}Nb_2O_5F_2$). At a wavelength of 450 nm, Δj is about 50 times higher in the Sn substituted materials compared to that observed in the Sn free corresponding compounds. The evolution of the photocurrent Δj with the intensity of the luminous flux (λ = 450 nm; V = 0.8V *vs.* Ag/AgCl) is shown in **Figure S8a** and **Figure S8b**. The photo-current density measured follows a power law ($\Delta j=\alpha\phi^n$) with n ≈ 0.65 and 0.57 for $SnNb_2O_5F_2$ and $SnTa_2O_5F_2$ respectively (see **Figure S8c** and **Figure S8d**). This behavior might reflect the rather large concentration of structural defects such as O^{2-}/F^- disorder as well as Sn/□ disorder that may act as photo-electron traps within the structure.[38] Finally, the evolution of the photocurrent with the V_{bias} (λ = 450 nm; Φ = 126 mW) is displayed in the **Figure S8e** and **Figure S8f**. It shows that although the applied potential enhances the Δj response, significant photocurrents of *ca.* 1.2 µA/cm² for $SnNb_2O_5F_2$ and *ca.* 0.2/cm² µA for $SnTa_2O_5F_2$ are measured without applying any voltage.

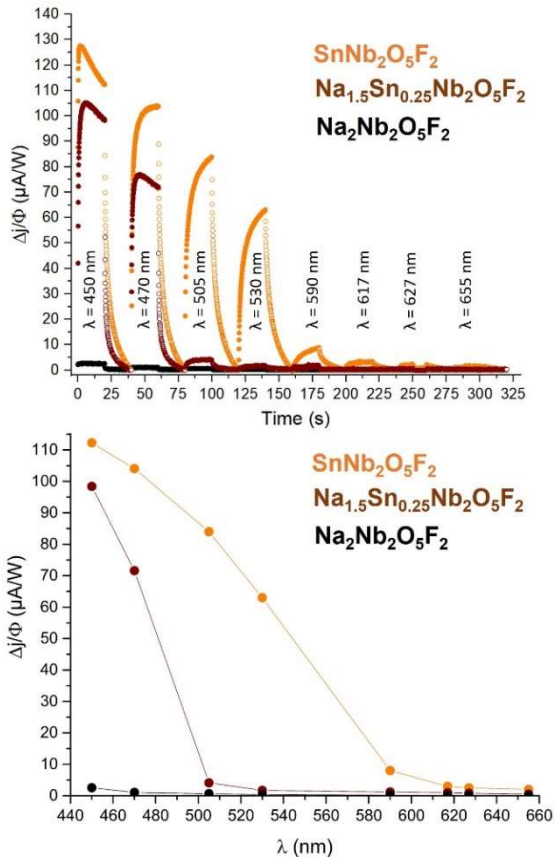

Figure 7: Photocurrent density as a function of wavelength in $Na_{2-2x}Sn_xNb_2O_5F_2$ (Φ=20mW/cm², Vbias = 0.8 V vs. Ag/AgCl in a 0.1 M aqueous solution of Na_2SO_4 as electrolyte).

Conclusion

We obtained several new pyrochlores (*i.e.* $Na_{2-2x}Sn_xM_2O_5F_2$ with M=Nb^{5+} or Ta^{5+} and 1 < x < 0) by ion-exchange reaction from $Na_2M_2O_5F_2$. Rietveld refinement of the structures reveals the Sn^{2+} lone pair stereochemical activity while UV-vis diffuse reflectance indicates a significant narrowing of the band gap. This is supported by electron localization function that allows to visualize the lone pair expression associated to the Sn^{2+} off-centering and the PDOS showing additional states, at the top of the valence band, mainly composed of a Sn 5s – Sn 5p hybridization through the F 2p orbitals while O 2p more weakly contribute. This gives rise to an unconventional situation where, despite their higher electro-negativity, the F 2p electrons are in average closer to the Fermi level than the O 2p, which is related to the particular case of the lone pair expression where the more ionic anion is known to enhance it. The band edge positions of $Na_{2-2x}Sn_xM_2O_5F_2$ materials encompass the thermodynamic redox potential of H^+/H_2 and O_2/H_2O, but the valence band of $SnNb_2O_5F_2$ could not be oxidative enough to overcome the overpotential associated to the O^{2-} oxidation. Hence it could be unsuitable for overall water splitting photocatalysis in contrast with $Na_{1.5}Sn_{0.25}Nb_2O_5F_2$. The photoconduction response of the Sn containing materials is *ca.* 50 times higher compared with corresponding Sn-free phases. Finally, this study shows that combining the beneficial effects of anionic O^{2-}/F^- mixing and lone pair stereochemical activity in pyrochlore structures is an efficient strategy for the design of OWS photocatalysts thanks to not only band gap but also band edge positions engineering.

Supporting information

Sn/M ratio obtained from X-ray fluorescence (XRF) spectroscopy, TGA - MS of $SnNb_2O_5F_2$ and $SnTa_2O_5F_2$ under Ar flow, electron diffraction pattern of $SnNb_2O_5F_2$ and $SnTa_2O_5F_2$, observed Fourier maps of $SnNb_2O_5F_2$ and $SnTa_2O_5F_2$, Rietveld refinements as well as refined parameters and agreement factors for $Na_1Sn_{0.5}Ta_2O_5F_2$ and $SnTa_2O_5F_2$, BVS obtained from the relaxed DFT structures of $SnNb_2O_5F_2$ and $SnTa_2O_5F_2$, Projected Density of States of $SnTa_2O_5F_2$, fit of the diffuse reflectance spectra using the Zanatta's method, photocurrent density as a function of wavelength for $Na_2Ta_2O_5F_2$, $Na_1Sn_{0.5}Ta_2O_5F_2$ and $SnTa_2O_5F_2$, photocurrent density as a function of flux for all materials.

Acknowledgement

This work was supported by the I-Site (ANR-16-IDEX-0004 ULNE) and by the Région Hauts-de-France (STaRS, accueil de jeunes chercheurs d'avenir). MSPD staff of ALBA is acknowledged for collecting data through in-house beamtime (proposal ID 2021035158). The TEM and XRD facilities are supported by the Conseil Régional des Hauts-de-France, and the European Regional Development Fund (ERDF), CNRS and Ministère de l'Education Nationale, de l'Enseignement Supérieur et de la Recherche. The DIM 1 "Energetic efficiency" of the UArtois is thanked for its financial support for photoelectrochemical measurements.

References

(1) Sato, S.; White, J. M. Photodecomposition of Water over Pt/TiO2 Catalysts. *Chem. Phys. Lett.* **1980**, *72* (1), 83–86. https://doi.org/10.1016/0009-2614(80)80246-6.

(2) Sayama, K.; Arakawa, H. Effect of Na2CO3 Addition on Photocatalytic Decomposition of Liquid Water over Various Semiconductor Catalysis. *J. Photochem. Photobiol. A Chem.* **1994**, *77* (2–3), 243–247. https://doi.org/10.1016/1010-6030(94)80049-9.

(3) Domen, K.; Naito, S.; Soma, M.; Onishi, T.; Tamaru, K. Photocatalytic Decomposition of Water Vapour on an NiO-SrTiO3 Catalyst. *J. Chem. Soc. Chem. Commun.* **1980**, No. 12, 543–544. https://doi.org/10.1039/C39800000543.

(4) INOUE, Y.; NIIYAMA, T.; ASAI, Y.; SATO, K. Stable Photocatalytic Activity of BaTi. *J. Chem. Soc. Chem. Commun.* **1992**, No. 7, 579–580.

(5) Sayama, K.; Arakawa, H. Effect of Carbonate Addition on the Photocatalytic Decomposition of Liquid Water over a ZrO2 Catalyst. *J. Photochem. Photobiol. A Chem.* **1996**, *94* (1), 67–76. https://doi.org/10.1016/1010-6030(95)04204-0.

(6) Kato, H.; Asakura, K.; Kudo, A. Highly Efficient Water Splitting into H2 and O2 over Lanthanum-Doped NaTaO3 Photocatalysts with High Crystallinity and Surface Nanostructure. *J. Am. Chem. Soc.* **2003**, *125* (10), 3082–3089. https://doi.org/10.1021/ja027751g.

(7) Kageyama, H.; Hayashi, K.; Maeda, K.; Attfield, J. P.; Hiroi, Z.; Rondinelli, J. M.; Poeppelmeier, K. R. Expanding Frontiers in Materials Chemistry and Physics with Multiple Anions. *Nat. Commun.* **2018**, *9* (1), 772. https://doi.org/10.1038/s41467-018-02838-4.

(8) Nakamura, R.; Tanaka, T.; Nakato, Y. Oxygen Photoevolution on a Tantalum Oxynitride Photocatalyst under Visible-Light Irradiation: How Does Water Photooxidation Proceed on a Metal-Oxynitride Surface? *J. Phys. Chem. B* **2005**, *109* (18), 8920–8927. https://doi.org/10.1021/jp0501289.

(9) Wang, Q.; Nakabayashi, M.; Hisatomi, T.; Sun, S.; Akiyama, S.; Wang, Z.; Pan, Z.; Xiao, X.; Watanabe, T.; Yamada, T.; Shibata, N.; Takata, T.; Domen, K. Oxysulfide Photocatalyst for Visible-Light-Driven Overall Water Splitting. *Nat. Mater.* **2019**, *18* (August), 1–8. https://doi.org/10.1038/s41563-019-0399-z.

(10) Kabbour, H.; Sayede, A.; Saitzek, S.; Lefèvre, G.; Cario, L.; Trentesaux, M.; Roussel, P. Structure of the Water-Splitting Photocatalyst Oxysulfide α-LaOInS 2 and Ab Initio Prediction of New Polymorphs. *Chem. Commun.* **2020**, *3*, 1645–1648. https://doi.org/10.1039/c9cc09797j.

(11) Vonrüti, N.; Aschauer, U. Band-Gap Engineering in AB(OxS1-x)3 Perovskite Oxysulfides: A Route to Strongly Polar Materials for Photocatalytic Water Splitting. *J. Mater. Chem. A* **2019**, *7* (26), 15741–15748. https://doi.org/10.1039/c9ta03116b.

(12) Kuriki, R.; Ichibha, T.; Hongo, K.; Lu, D.; Maezono, R.; Kageyama, H.; Ishitani, O.; Oka, K.; Maeda, K. A Stable, Narrow-Gap Oxyfluoride Photocatalyst for Visible-Light Hydrogen Evolution and Carbon Dioxide Reduction. *J. Am. Chem. Soc.* **2018**, *140* (21), 6648–6655. https://doi.org/10.1021/jacs.8b02822.

(13) Luo, Y.; Zhou, X.; Zhang, J.; Qi, Y.; Li, Z.; Zhang, F.; Li, C. Development of Sn2+-Based Oxyfluoride Photocatalyst with Visible Light Response of ca. 650 Nm via Strengthened Hybridization of Sn 5s and O 2p Orbitals. *J. Energy Chem.* **2021**, No. xxxx. https://doi.org/10.1016/j.jechem.2021.07.028.

(14) Giampaoli, G.; Li, J.; Hermann, R. P.; Stalick, J. K.; Subramanian, M. A. Tuning Color through Sulfur and Fluorine Substitutions in the Defect Tin(II, IV) Niobate Pyrochlores. *Solid State Sci.* **2018**, *81*, 32–42. https://doi.org/10.1016/j.solidstatesciences.2018.05.001.

(15) Oka, K.; Hojo, H.; Azuma, M.; Oh-Ishi, K. Temperature-Independent, Large Dielectric Constant Induced by Vacancy and Partial Anion Order in the Oxyfluoride Pyrochlore Pb2Ti2O6-ΔF2δ. *Chem. Mater.* **2016**, *28* (15), 5554–5559. https://doi.org/10.1021/acs.chemmater.6b02509.

(16) Hosogi, Y.; Kato, H.; Kudo, A. Photocatalytic Activities of Layered Titanates and Niobates Ion-Exchanged with Sn2+ under Visible Light Irradiation. *J. Phys. Chem. C* **2008**, *112* (45), 17678–17682. https://doi.org/10.1021/jp805693j.

(17) Boivin, E.; Pourpoint, F.; Saitzek, S.; Simon, P.; Roussel, P.; Kabbour, H. An Unusual O2-/F-Distribution in the New Pyrochlore Oxyfluorides: Na2B2O5F2(B = Nb, Ta). *Chem. Commun.* **2022**, *58* (14), 2391–2394. https://doi.org/10.1039/d1cc06760e.

(18) Fauth, F.; Peral, I.; Popescu, C.; Knapp, M. The New Material Science Powder Diffraction Beamline at ALBA Synchrotron. *Powder Diffr.* **2013**, *28*, 360–370.

(19) Rodriguez-carvajal, J. Recent Advances in Magnetic Structure Determination by Neutron Powder Diffraction. *Phys. B* **1993**, *192*, 55–69.

(20) Zanatta, A. R. Revisiting the Optical Bandgap of Semiconductors and the Proposal of a Unified Methodology to Its Determination. *Sci. Rep.* **2019**, *9* (1), 11225. https://doi.org/10.1038/s41598-019-47670-y.

(21) Bloch, P. E. Projector Augmented-Wave Method. *Phys. Rev. B* **1994**, *50* (24), 17954–17979.

(22) Joubert, D. From Ultrasoft Pseudopotentials to the Projector Augmented-Wave Method. *Phys. Rev. B - Condens. Matter Mater. Phys.* **1999**, *59* (3), 1758–1775. https://doi.org/10.1103/PhysRevB.59.1758.

(23) Kresse, G.; Furthmüller, J. Efficiency of Ab-Initio Total Energy Calculations for Metals and Semiconductors Using a Plane-Wave Basis Set. *Comput. Mater. Sci.* **1996**, *6* (1), 15–50. https://doi.org/10.1016/0927-0256(96)00008-0.

(24) Perdew, J. P.; Burke, K.; Ernzerhof, M. Generalized Gradient Approximation Made Simple. *Phys. Rev. Lett.* **1996**, *77* (18), 3865–3868.

(25) Silvi, B.; Savin, A. Classification of Chemical Bonds Based on Topological Analysis of Electron Localization Functions. *Nature*. 1994, pp 683–686. https://doi.org/10.1038/371683a0.

(26) Uma, S.; Singh, J.; Thakral, V. Facile Room Temperature Ion-Exchange Synthesis of Sn2+ Incorporated Pyrochlore-Type Oxides and Their Photocatalytic Activities. *Inorg. Chem.* **2009**, *48* (24), 11624–11630. https://doi.org/10.1021/ic901658w.

(27) Vanderah, T. A.; Levin, I.; Lufaso, M. W. An Unexpected Crystal-Chemical Principle for the Pyrochlore Structure. *Eur. J. Inorg. Chem.* **2005**, No. 14, 2895–2901. https://doi.org/10.1002/ejic.200500234.

(28) Brown, I. D.; Altermatt, D. Bond-Valence Parameters Obtained from a Systematic Analysis of the Inorganic Crystal Structure Database I . *Acta Cryst* **1985**, *41*, 244–247.

(29) Art, D. J. S.; Meads, R. O. Y. E.; Parker, G. Pyrochlores . IX . Partially Oxidized Sn2Nb20 , and Sn , Ta , O ,: A Miissbauer Study of Sn (I1 , IV) Compounds1 Results Identification of the Mossbauer Absorption Peaks Apart from Varying Relative Intensities The. *Can. J. Chem.* **1972**, *51*, 1041.

(30) Shannon, R. D.; Prewitt, C. T. Effective Ionic Radii in Oxides and Fluorides. *Acta Crystallogr. Sect. B Struct. Crystallogr. Cryst. Chem.* **1969**, *25* (5), 925–946. https://doi.org/10.1107/s0567740869003220.

(31) Walsh, A.; Watson, G. W. Influence of the Anion on Lone Pair Formation in Sn(II) Monochalcogenides: A DFT Study. *J. Phys. Chem. B* **2005**, *109* (40), 18868–18875. https://doi.org/10.1021/jp051822r.

(32) Walsh, A.; Payne, D. J.; Egdell, R. G.; Watson, G. W. Stereochemistry of Post-Transition Metal Oxides: Revision of the Classical Lone Pair Model. *Chem. Soc. Rev.* **2011**, *40* (9), 4455–4463. https://doi.org/10.1039/c1cs15098g.

(33) Le Berre, F.; Crosnier-Lopez, M. P.; Galven, C.; Fourquet, J. L.; Legein, C.; Body, M.; Buzaré, J. Y. Ca2+/Vacancies and O2−/F− Ordering in New Oxyfluoride Pyrochlores Li2xCa1.5−x□0.5−xM2O6F (M = Nb, Ta) for 0 ≤ x ≤ 0.5. *Dalt. Trans.* **2007**, *23*, 2457–2466. https://doi.org/10.1039/b701863k.

(34) Huang, S.; Wang, C.; Sun, H.; Wang, X.; Su, Y. Steering Charge Kinetics of Tin Niobate Photocatalysts: Key Roles of Phase Structure and Electronic Structure. *Nanoscale Res. Lett.* **2018**, *13*. https://doi.org/10.1186/s11671-018-2578-2.

(35) Aiura, Y.; Ozawa, K.; Hase, I.; Bando, K.; Haga, H.; Kawanaka, H.; Samizo, A.; Kikuchi, N.; Mase, K. Disappearance of Localized Valence Band Maximum of Ternary Tin Oxide with Pyrochlore Structure,

Sn2Nb2O7. *J. Phys. Chem. C* **2017**, *121* (17), 9480–9488. https://doi.org/10.1021/acs.jpcc.6b12572.

(36) Kudo, A.; Kato, H.; Nakagawa, S. Water Splitting into H2 and O2 on New Sr2M2O7 (M = Nb and Ta) Photocatalysts with Layered Perovskite Structures: Factors Affecting the Photocatalytic Activity. *J. Phys. Chem. B* **2000**, *104* (3), 571–575. https://doi.org/10.1021/jp9919056.

(37) Kalanur, S. S. Structural, Optical, Band Edge and Enhanced Photoelectrochemical Water Splitting Properties of Tin-Doped WO3. *Catalysts* **2019**, *9* (5). https://doi.org/10.3390/catal9050456.

(38) Ullrich, B.; Xi, H. Photocurrent Limit in Nanowires. *Opt. Lett.* **2013**, *38* (22), 4698. https://doi.org/10.1364/ol.38.004698.